Programmable shaping of ultrabroad-bandwidth pulses from a Ti:sapphire laser

A. Efimov, C. Schaffer, and D. H. Reitze

Department of Physics, The University of Florida, Gainesville, Florida 32611

Received January 3, 1995; revised manuscript received April 21, 1995

We have used a commercially available liquid-crystal spatial light modulator within a reflective optics pulse-shaping apparatus to shape ultrashort pulses with temporal resolution approaching 10 fs. Using the spatial light modulator as a phase modulator, we produce a variety of complex ultrafast waveforms, including odd pulses, high repetition rate (>23 THz) pulse trains, and asymmetric pulse trains. We also show that it is possible to compensate for large amounts of high-order phase dispersion (in excess of 60π) by appropriate cubic- and quartic-phase modulations of the pulse. Finally, we examine the limitations of shaping ultrabroad-bandwidth pulses. We find that, for specific classes of waveforms, Fourier-transform pulse-shaping techniques can be used for pulses with 5-fs durations, which exceed the current state of the art in ultrashort pulse generation. However, synthesis of general waveforms with 5-fs resolution will require compensating for nonlinear spatial dispersion of frequency in the masking plane.

1. INTRODUCTION

Pulse shaping within a dispersion-free grating–lens apparatus has proved to be a powerful method for synthesizing complex femtosecond optical waveforms. In this method, which was first developed in the femtosecond regime by Weiner *et al.*,[1] an optical pulse is first transformed from the time domain into the frequency domain. A frequency-dependent complex linear filter that modifies the spectrum of the pulse is then applied. Finally, the pulse is transformed back into the time domain. The resulting output pulse has a temporal field profile that is essentially the Fourier transform of the frequency filter imposed on the electric-field spectrum of the pulse.

The ability to shape pulses has led to many applications in the fields of physics and chemistry, such as the observation of the fundamental dark soliton in optical fiber[2] and mode-selective excitation of coherent phonons.[3] A particularly powerful application of femtosecond pulse shaping is the dynamic control of molecular and chemical systems[4–6] in which the goal is to drive a system into a user-specified final quantum state by use of tailored optical fields to interact coherently with and to manipulate the dynamic evolution of the system. Experimental demonstrations thus far include control of the evolution of an electronic wave packet in molecular iodine.[7] Recently, new proposals have been put forth for extending these ideas into solid-state electronics and optoelectronics.[8–10] Appropriately designed optical or electrical fields could be used to control the evolution of electron-hole distributions in a multiple quantum well or a superlattice. In addition, it has recently been shown that a complex chirped-pulse train can resonantly excite large-amplitude plasma oscillations and laser wake fields.[11] The use of shaped laser pulses as wake-field drivers may lead to a new class of laser-based charged particle accelerators.

Initial femtosecond pulse-shaping efforts employed masks that were lithographically patterned on fixed substrates that, although providing shaped pulses of extremely high fidelity, were experimentally cumbersome in that they required mask replacement and realignment each time a new waveform was desired.[1] Within recent years, several innovations have been developed that have improved both the ease and the versatility with which pulses can be shaped. Most notably, the use of dynamically reconfigurable filters (masks) has been demonstrated by a number of groups as a way of introducing real-time programmability of shaped pulses. These methods include the use of a single liquid-crystal modulator within a pulse shaper, which can alter either phase or amplitude independently,[12] the use of two liquid-crystal modulators within a modified pulse shaper, which provide independent control of both phase and amplitude,[13] and, most recently, the use of an acousto-optic modulator within a pulse-shaping apparatus, which can simultaneously modulate phase and amplitude.[14] Each of these methods has been applied with success to pulses with durations of greater than 70 fs. More complex optical processing and waveform synthesis (convolution and time-to-space conversion) have been demonstrated by the use of spectral holographic techniques.[15–17] Phase-only filtering has been demonstrated on pulses as short as 20 fs.[18] However, only fixed masks were used. Although these experiments demonstrated that it was possible to shape pulses on these time scales, the fidelity of the shaped pulses was compromised somewhat by the quality of the input pulses, which were generated by the use of spatial soliton pulse compression techniques.[19] The development of mode-locked Ti:sapphire lasers now affords us the opportunity to extend these methods to pulses that approach 10 fs in duration and, in particular, to explore the limits imposed by such short-duration, ultrabroad-bandwidth optical pulses. With current laser technology, it is now possible to produce pulses as short as

0740-3224/95/101968-13$06.00

8.6 fs in duration directly from a laser oscillator.[20] Such a pulse has only three oscillations of the electromagnetic field and begins to approach the theoretical limitation of a single-cycle pulse.

In this paper we extend spectral-domain pulse-shaping techniques to ultrabroad-bandwidth pulses and explore the limitations inherent in tailoring ultrashort waveforms. In particular, we demonstrate the use of a commercially available liquid-crystal one-dimensional spatial light modulator (SLM) in a pulse shaper to synthesize a variety of complex ultrafast waveforms with resolution approaching 10 fs. There are two important motivations for extending pulse-shaping techniques into pulse-width regimes of 10 fs and less.

First, the manipulation and control of frequency-dependent phase dispersion has long been recognized as one of the methods for generating and propagating ultrashort pulses. For ultrabroad-bandwidth pulses, it is critical to minimize phase distortions (cubic and higher-order phase dispersion) and to maintain a constant phase across the entire frequency spectrum as pulses propagate through dispersive elements. Adjustable frequency-domain pulse-shaping methods such as these are ideally suited for compensating for phase distortions and could potentially be incorporated directly into laser cavities that are currently limited by fourth-order phase.[21] Similar difficulties exist on a much larger scale in chirped-pulse amplifiers,[22–24] which incorporate rudimentary pulse shaping in the form of stretchers and compressors. Recently it has been recognized that the residual higher-order phase that is imparted to the pulse can compromise the width and the fidelity of pulses that are 100 fs in duration[25] and is particularly problematic when one attempts to amplify 20-fs pulses.[26] As we show below, the use of programmable pulse-shaping techniques gives us the capability to control large cubic- and quartic-phase shifts arbitrarily and independently. Moreover, the use of a programmable pulse shaper in the amplitude mode can be used to shape input pulse spectrums dynamically to overcome the effects of gain narrowing in chirped-pulse amplifier systems.[24]

Second, the ability to tailor waveforms with resolution nearing that of the underlying carrier frequency represents an important advance in achieving the goal of quantum optimal control of complex molecular systems.[4] Quantum optimal control computations performed on realistic complex molecules suggest that it is possible to achieve novel, physically interesting target final states (control of bond stretching, vibrational amplitudes, and bond-selective dissociation) by the use of shaped visible and infrared lasers as controllers. One key finding of theoretical investigations is that, in order to achieve specific target states, phase and amplitude control of the optical field must be exercised at the scale of the carrier frequency. Here, we manipulate optical fields that are 13 fs in duration and have only five field cycles.

This paper is organized in the following manner. In Section 2, we give a description of the apparatus and details pertinent to our experiments. The results of our experiments in which phase filtering is used are presented in Section 3, in which we display various synthesized waveforms, including odd pulses, pulse trains with repetition rates in excess of 23 THz, and asymmetric pulse trains produced from masks with gray-level phase control. The use of a pulse shaper as a high-order phase compensator is presented in Section 4. Here we show that independently adjustable cubic- and quartic-phase profiles (in excess of 60π) can be imparted with a negligible compromise of pulse fidelity. A general discussion of the difficulties associated with shaping 13-fs pulses is presented in Section 5, including the effects of phase and spatial dispersion of the frequency components. In particular, we theoretically consider how well these methods work on pulses much shorter than those used here. We conclude in Section 6.

2. EXPERIMENTAL METHODS

All our pulse-shaping experiments were performed with a commercially available one-dimensional liquid-crystal SLM (Meadowlark Optics SLM2256), which is described in more detail below. Our pulse shaper, which is similar in design to that previously used in shaping a 20-fsec pulse, is shown in Fig. 1. It consists of a pair of 600 line/mm gratings placed at the focal planes of a unit-magnification confocal pair of concave 12.5-cm focal-length gold spherical mirrors. Midway through the apparatus, the optical frequencies are spatially separated, with a linear spatial dispersion given by $dx/d\lambda \approx f/(d \cos \theta_d) \approx 0.085$ mm/nm, where f is the focal length, d is the grating period, $\theta_d = 28.1°$ is the diffraction angle, and x is the position of each frequency component in the masking plane. Because our shaper is designed to accommodate 130 nm (which corresponds to a 12-mm-wide spectrum at the masking plane), the spatial dispersion exhibits a 6% wavelength variation over the bandwidth of the pulse. We consider these effects in more detail in Section 5. In constructing our shaper, we selected a spectral window that truncated at approximately six e-foldings of the maximum intensity.

For these studies, we used a dispersion-compensated mode-locked Ti:sapphire laser with a short (4.5-mm) Ti:sapphire crystal, similar to the design of Asaki *et al.*[27] Average output powers of 200 mW for 4.5-W pump power were obtained after the beam was double passed through an extra-cavity prism sequence. For most of our experiments, pulse durations were measured in a noncollinear

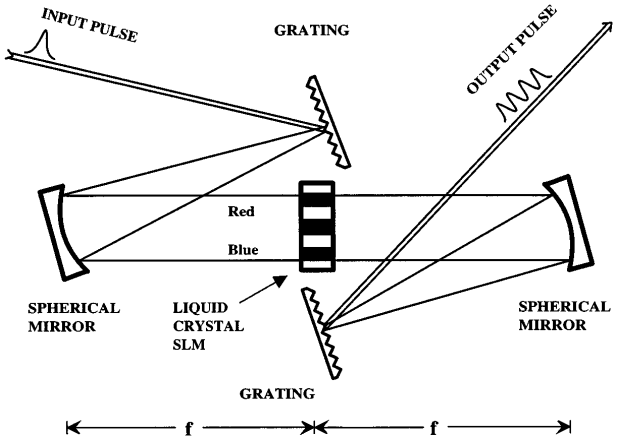

Fig. 1. Schematic of the ultrabroad-bandwidth pulse-shaping apparatus.

autocorrelator consisting of balanced scanning and reference arms, a focusing mirror, and a 0.1-mm-thick KDP crystal. We routinely measured pulse widths in the range of 12–14 fs (sech^2 pulse shape).

The modulator consists of 128 individually addressable elements 100 μm wide by 500 μm high with a 2-μm gap between each pixel for an effective window of 13 mm. The liquid-crystal pixels are mounted in a 4.6-mm-thick fused-silica housing. Driver circuitry supplied by the manufacturer provided independent voltage control with 12-bit resolution. An important consideration in our experiments was the variation of phase as a function of wavelength. Phase shifts in excess of 2π at all wavelengths are required for utilizing the full capability of the pulse shaper. We therefore performed calibration of the modulator at 750-, 800-, and 850-nm wavelengths that effectively span the mode-locked spectrum of the pulse. We accomplished this by placing the modulator between two crossed Glan–Thompson polarizers whose polarization angles were oriented $\pm 45°$ with respect to the slow (vertical) axis of the liquid crystal. The beam diameter of $\sim$300 μm resulted in averaging of the phase over three pixels. The transmission of the beam was then recorded as a function of voltage applied to the modulator. The theoretical transmission for our vertically input polarized beam can be easily computed by the use of Jones matrices[28] and is given by

$$\Delta\phi(V_p) = \cos^{-1}\left[1 - 2\,\frac{I_{\text{trans}}(V_p)}{I_{\text{in}}}\right], \tag{1}$$

where $\Delta\phi$ is the voltage-dependent phase difference between the slow and the fast axes of the modulator, V_p is the pixel applied voltage, and I_{trans} and I_{in} are the transmitted and the input intensities, respectively. Figure 2 displays the phase change for the three wavelengths. Maximum phase shifts in excess of 2π were obtained at all wavelengths. The maximum phase shift was measured to be almost 3π at 750 and 800 nm with an effective gray-level resolution of approximately 2000, which corresponds to a phase resolution of <2 mrad. More significantly, we found uniformity of phase shift in the range of 0 to 2π for all wavelengths with an approximately linear response from 0 to 1.5π. The negligible difference in phase shift between 750 to 800 nm is somewhat surprising, as $\Delta\phi = 2\pi n(V_p)L/\lambda$ scales inversely with wavelength. The lower saturation value ($\sim 2.5\pi$) of the phase shift at 850 nm is qualitatively (but not quantitatively) consistent with this scaling. We also tested pixel uniformity of the device at a single wavelength by operating the modulator at a fixed voltage and scanning across the pixels. Slight variations in transmitted intensity ($<5\%$) were observed.

Spectra of the shaped pulses were measured with a 0.3-m spectrometer and linear photodiode array. Temporally shaped pulse profiles were measured with standard noncollinear cross-correlation techniques. A small portion of the beam was split off to serve as the reference. After traversing the shaper, the beams were mixed in a 0.1-mm KDP crystal. Because of the high repetition rate and average power of the Ti:sapphire laser, we were able to obtain all our data in single scans. Figure 3 displays a cross correlation of an unshaped pulse propagating through the shaper (solid curve) and the intensity autocorrelation of the laser. The autocorrelation widths and the cross-correlation widths are 19.8 and 20.3 fs, respectively. Note that the wings of the cross correlation are diminished with respect to the autocorrelation. This is due to a reduction in the amount of excess cubic phase as the pulse propagates through the shaper. We discuss the effects of high-order phase in more detail in Section 5.

3. PHASE FILTERING OF ULTRABROAD-BANDWIDTH PULSES

As an initial test of our capabilities, we chose to synthesize simple temporal pulse profiles with the SLM operated as a phase filter. In this configuration, the incoming light is polarized vertically, along the slow axis of the liquid-crystal modulator. Approximately 33% of the input beam was transmitted through the shaper, with losses predominantly from zeroth- and second-order diffractions from the grating.[5] Some difference in throughput was measured with the biased SLM in the shaper. Owing to the uniformity of the SLM phase response, a single phase-to-voltage calibration was used for all wavelengths. This greatly simplified the generation of masks in our experiments.

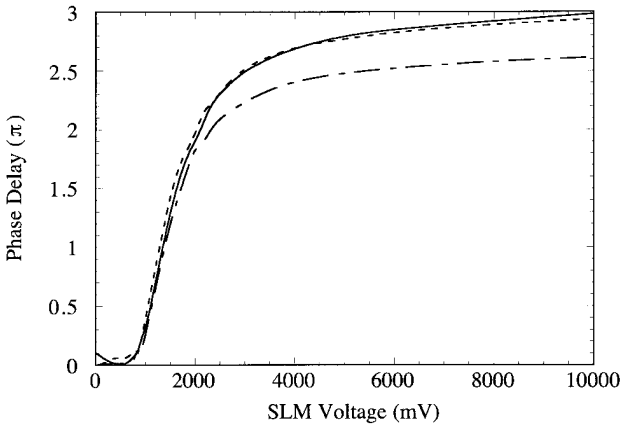

Fig. 2. Phase versus voltage calibration for the liquid-crystal SLM for 750 nm (solid curve), 800 nm (dashed curve), 850 nm (short-and-long-dashed curve). Phase shifts in excess of 2π can be obtained at all wavelengths.

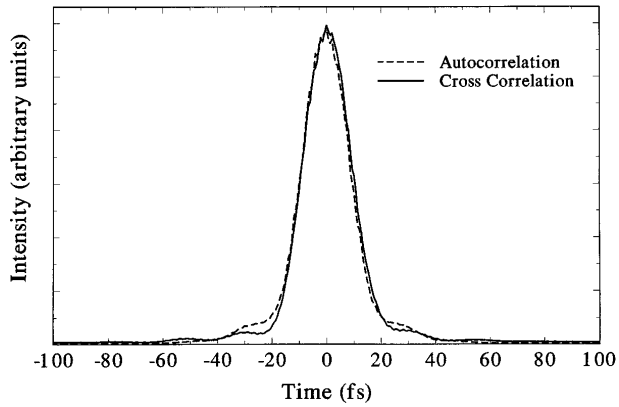

Fig. 3. Cross correlation (solid curve) of an unshaped pulse after it propagates through the shaper. The (sech^2) deconvolved pulse width is 13.0 fs. For comparison, an autocorrelation directly from the oscillator is displayed (dashed curve).

One of the simplest pulses that can be synthesized by pure phase filtering is the odd pulse. The odd pulse is generated when a π-phase shift of the carrier frequency is imposed in the center of a symmetric spectrum. The term odd pulse reflects the antisymmetric functional dependence of the electric-field envelope on time and is a special type of the zero-area (0π) pulse, which is of fundamental significance in the field of coherent optics.[29] The resonant interaction of an odd pulse with a two-level atom results in an initial excitation from the ground state to the excited state during the leading part of the pulse followed by deexcitation back to the ground state during the latter part of the pulse as a result of the abrupt π-phase shift. Odd pulses could also prove useful for enhancing terahertz emissions from asymmetric coupled quantum wells.[10] A cross correlation of an odd pulse generated from a 13-fs pulse is shown in Fig. 4. Unlike a pure odd pulse, which possesses a symmetric intensity profile, our pulse displays a slight asymmetry in the widths of the peaks. These deviations come from primarily two sources. First, the frequency spectrum of the Ti:sapphire laser is not symmetric and therefore does not truly conform to the criteria for an odd pulse. In addition, uncompensated cubic- and quartic-phase dispersions from the SLM are present in the shaped output pulse. Nevertheless, the overall fidelity of the odd pulse is excellent.

Another simple but powerful phase filter for generating a train of equally spaced pulses is based on so-called maximal length sequences[30] (M-sequences). This method has previously been used to generate pulse trains with repetition rates of up to 12.5 THz.[18] Pulse trains such as these have been used as a means of exciting optical phonon modes in molecular crystals by impulse-stimulated Raman scattering.[3] These masks are binary-phase masks whose phase response is periodic with a period corresponding to a frequency δF. Each period is divided into P pixels, with the phase of each pixel given by either 0 or $\Delta\phi(V) = 2\pi n(V_p)L/\lambda$, as determined by the M-sequence, where L is the optical path of the pixel and $n(V_p)$ is the SLM-induced index change. The output pulse train then consists of a series of P individual pulses under a Gaussian envelope with repetition rate δF. For these experiments, we used the length 7 M-sequence $\{\Delta\phi, \Delta\phi, 0, \Delta\phi, 0, 0, 0\}$ with $\Delta\phi = 1.1\pi$. Our results are shown in Fig. 5, which displays cross correlations of pulse trains with repetition periods of 8.8 THz [Fig. 5(a)], 16.0 THz [Fig. 5(b)], and 23.6 THz [Fig. 5(c)]. We note that 23.6 THz is, to our knowledge, the highest modulation frequency ever imposed on a lightwave by the use of linear-filtering techniques. Both the 8.8- and 16.0-THz trains have well-resolved individual pulses. Pulses in the 23.6-THz train are not as well resolved, but individual pulses are clearly evident. The choice of periodicities was dictated by fixed pixel sizes and fixed spectral dispersion in the Fourier plane of the shaper. Neglecting higher-order spatial dispersion in the mask plane, each SLM pixel accommodates a bandwidth of $d\omega/dx\Delta x_{\text{pixel}} = 0.47$ THz. A repetition of M pixels should result in pulse trains that have repetition rates of an integer multiple of $0.47M$ THz, the length of the M-sequence multiplied by the bandwidth of one pixel. Continuous adjustment of the spatial frequency dispersion in the Fourier plane requires either adjusting the diffraction angle of the shaper gratings or incorporating adjustable focal-length (telescoping) optics with the shaper. Note, however, that the repetition periods of the pulse trains generated in these experiments are not simple integer multiples of each other, because higher-order spatial dispersion slightly modifies the repetition period of the trains.

Many physical applications demand complex pulse shapes that, for example, possess asymmetric temporal profiles. As an example, impulsive resonant Raman excitation of large-amplitude (anharmonic) optical phonons requires tailoring an optical pulse train to first harmonically excite vibrational modes with a train of equispaced pulses and then, as the amplitude of the vi-

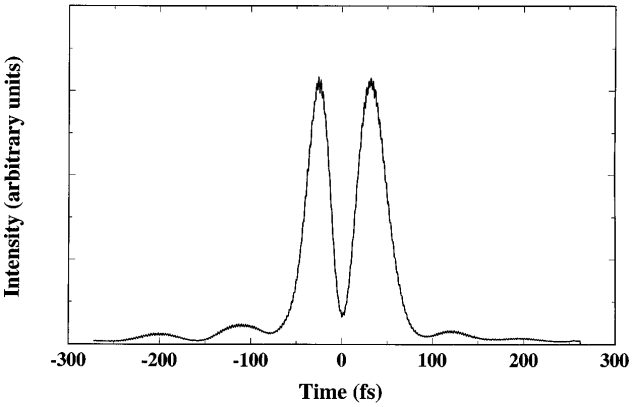

Fig. 4. Cross correlation of a 13-fs odd pulse. The high fidelity of this pulse is characterized by the depth of central minimum of the pulse.

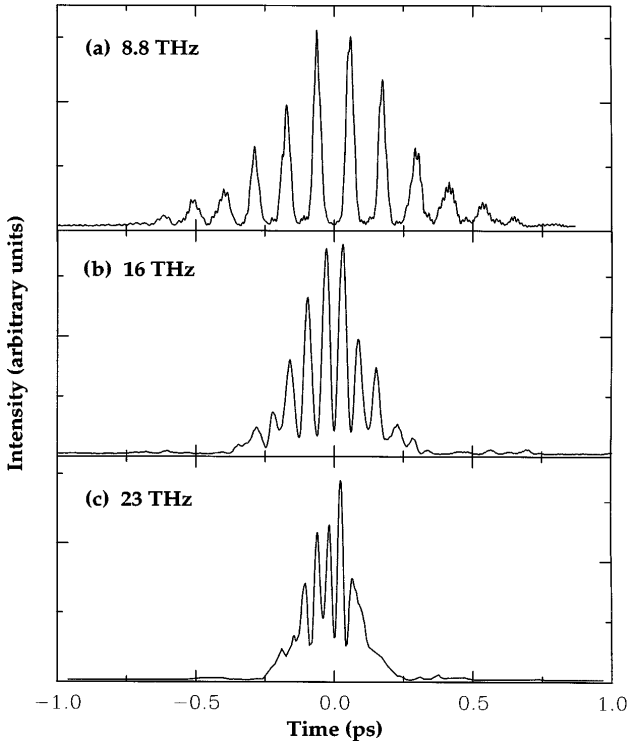

Fig. 5. Cross correlations of phase-filtered terahertz-rate pulse trains generated by length 7 M-sequences: (a) 8.8-THz train, (b) 16.0-THz train, (c) 23.6-THz train.

bration becomes sufficiently large, to follow the phonon out of the harmonic well by adjusting the interpulse spacing. Such pulse trains may also be useful in driving large-amplitude plasma oscillations in low-density laser-produced plasmas.[11] In principle, any arbitrarily shaped waveform can be synthesized if both phase and amplitude filtering can be implemented. The appropriate complex frequency filter is simply given by $M(\omega) = A(\omega)\exp[i\phi(\omega)] = E_{\text{out}}(\omega)/E_{\text{in}}(\omega)$. However, pure phase filtering is desirable when (i) both phase and amplitude filtering cannot be experimentally implemented, or (ii) the reduction in energy that necessarily accompanies amplitude filtering is undesirable. Binary-phase-only filters necessarily generate waveforms that have symmetric intensity profiles and cannot be used for the generation of more complex pulses. We therefore attempted to synthesize more complex (asymmetric) pulse trains by using gray-level phase masks. For these experiments, we designed phase filters by using simulated annealing optimization codes.[31] Simulated annealing methods have previously been used to design gray-level phase and amplitude filters successfully to overcome limitations of fixed SLM pixel size.[13] However, these methods met with limited success in synthesizing pure phase filters,[32] particularly when confronted with target pulses whose features deviated significantly from the input pulse on the time scale of the input pulse. We therefore adopted a modest strategy of selecting targets of the form

$$E_{\text{target}}(t) = u(t) * \sum_{k=-N}^{N} A_k \exp[i\alpha_k{}^{(2)}t^2]\delta(t - kT), \qquad (2)$$

i.e., targets that consist of trains of pulses in which the spacing between pulses or the pulse durations were varied. Here $u(t)$ is the field profile of an unshaped pulse, $0 \le A_k \le 1$ is real and defines the field amplitude for the pulse at time $t - kT$, $\alpha_k{}^{(2)} \sim \omega_0{}^2$ is the quadratic chirp parameter for the kth pulse, and $*$ is the convolution operator. We expect that filters generated by using optimization methods should be most physically effective in accurately positioning pulses within the train, as this depends only on the introduction of the appropriate phase delay at the appropriate portions of the pulse spectrum. Individual pulse amplitudes within the train are determined by the relative weight (energy) of the phase-shifted spectrum and therefore are sensitive to the exact amplitude profile of the input spectrum. Briefly, phase masks with 64 gray levels were randomly generated and multiplied with the experimentally measured input spectrum to generate an output field spectrum $E_{\text{guess}}(\omega) = E_{\text{in}}(\omega)\exp[i\phi_i(\omega)]$. The resulting temporal waveform $E_{\text{guess}}(t)$ was computed by an inverse Fourier transform on a 1024-element temporal grid and compared with a specified target waveform $E_{\text{target}}(t)$ by the computation of a simple cost functional J:

$$J[\Phi(\omega)] = \sum_{j=1}^{1024} |E_{\text{guess}}{}^2(t_j) - E_{\text{target}}{}^2(t_j)|, \qquad (3)$$

which minimizes the differences in intensity amplitude between the generated and the target fields. The minimization of J proceeds by the computation of $\Delta J = J_{\text{current}} - J_{\text{prev}}$, in which the current guess is always accepted if $\Delta J < 0$ and is accepted with probability $\exp(-\Delta J/T)$ if $\Delta J \ge 0$. The temperature T is initially set to a value well in excess of ΔJ. In this way, the cost function is initially free to move about its entire parameter space and seek out the global minimum. As the annealing proceeds, the temperature is reduced and the cost function descends into the global minimum.

Results for three different trains are shown in Fig. 6. The first [Fig. 6(a)] is a train of three pulses in which the amplitudes and the interpulse spacings are varied. The agreement between the target train (dashed curve), the numerically synthesized pulse train in which the optimal mask is used (dotted-dashed curve), and the experimental cross correlation (solid curve) is excellent, with slight deviations in the amplitudes (<10%) and positions (<5 fs) of the experimentally synthesized train. Approximately 92% of the initial pulse energy resides in the target pulses, in good agreement with numerical results. Because the theoretical plots have not been convolved with the original reference pulse, the slight temporal broadening is an artifact of the cross correlation. Figure 6(b) depicts a train of three equal amplitude pulses in which both interpulse spacings and pulse durations are varied. Again we find reasonably good agreement between the target and the cross correlation. Temporal positions agree to within <10 fs, and, with the exception of the first pulse in the train, pulse durations are within <10% of the target. In the worst case, the amplitudes vary by ~25% of the target value. Finally, in Fig. 6(c) we display a chirped-pulse train consisting of six replica pulses. Once again, we observe minimal

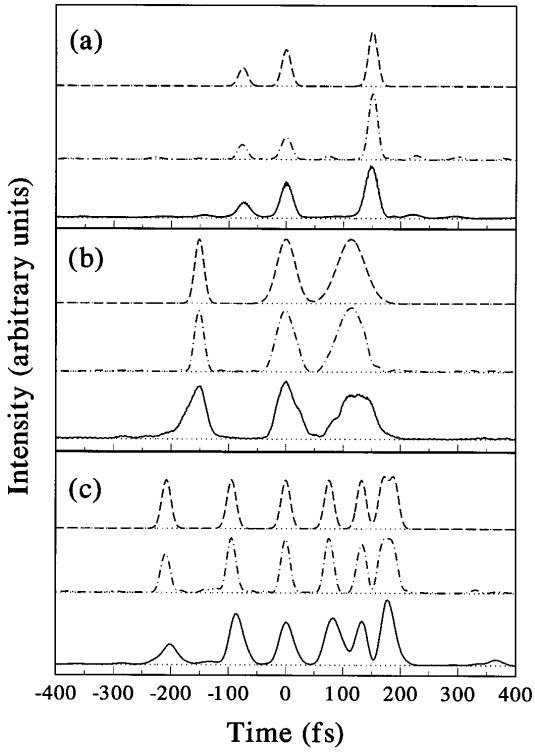

Fig. 6. Cross correlations of asymmetric, chirped trains of femtosecond pulses generated by 64 gray-level phase masks designed with simulated annealing. Each panel shows the target (dashed curve), the numerical results (dotted-dashed curve), and the experimental cross correlation (solid curve).

deviations (<10 fs) from the peak target pulse positions. Excluding the initial pulse, experimental cross-correlation amplitudes are within 15% of their target values. The initial pulse has a peak amplitude of approximately 40% of the target value, and slight variations in pulse durations are observed.

4. COMPENSATION OF CUBIC- AND QUARTIC-PHASE DISPERSIONS

Compensation of high-order phase dispersion in pulse-compression and pulse-amplification applications is another potential application of programmable pulse shaping. The propagation of ultrabroad-bandwidth pulses through dispersive media results in severe pulse broadening as frequency-dependent phase shifts accumulate. For optical pulses with spectra that are not too broad (i.e., that satisfy $\Delta\omega/\omega_0 \ll 1$), the phase of an optical pulse propagating through dispersive media can be conveniently expressed in a Taylor series as

$$\Phi(\omega) = \Phi(\omega_0) + \Phi^{(1)}(\omega)(\omega - \omega_0) + \frac{1}{2!}\Phi^{(2)}(\omega)(\omega - \omega_0)^2 + \frac{1}{3!}\Phi^{(3)}(\omega)(\omega - \omega_0)^3 + \frac{1}{4!}\Phi^{(4)}(\omega)(\omega - \omega_0)^4 + \ldots, \quad (4)$$

where ω_0 is the center frequency of the pulse and $\Phi^{(n)}(\omega) = (\mathrm{d}^n\Phi/\mathrm{d}\omega^n)_{\omega=\omega_0}$ is the nth-order derivative of the phase evaluated at ω_0. The group delay and the linear dispersion of an optical pulse are given by the linear term $\Phi^{(1)}$ and the quadratic term $\Phi^{(2)}$, respectively. Compensation of linear dispersion is normally accomplished through the use of grating or prism pairs[33,34]; however, for pulse compression of sub-10-fs pulses[35] or chirped-pulse amplification of sub-100-fs pulses,[26,36] cancellation of higher-order phase dispersion [$\Phi^{(3)}$, $\Phi^{(4)}$] is essential for optimizing the fidelity and the duration of the pulse. Methods for compensating for higher-order dispersion include the use of ray-tracing algorithms to design amplifiers in which phase dispersion cancels at each order[26] and the incorporation of adjustable air-spaced doublet lenses into stretchers that provide independent control of third- and fourth-order dispersions.[25] In this section, we show that large cubic-[$\Phi^{(3)}$] and quartic-[$\Phi^{(4)}$] phase shifts (over 120π) can be imprinted on pulses by the programmable pulse shaper.

We impart the cubic phase on a pulse by computing the frequency-dependent phase, $\Delta\Phi_{\mathrm{cubic}}(\omega) = (1/3!)\Phi^{(3)}(\omega_0)(\omega - \omega_0)^3$, and then mapping this onto the masking plane. Because the liquid-crystal SLM is restricted to phase shifts of 2π, larger phase shifts are accomplished when the phase is folded back into the range $-\pi \le \Delta\Phi \le \pi$; $\Delta\Phi_{\mathrm{fold}}(x) = \Delta\Phi_{\mathrm{cubic}}(x) - (2N + 1)\pi$. Moreover, because the SLM is pixelated, it cannot imprint a smooth continuous-phase profile. Instead, the spectrum is sampled by the modulator at discrete points, $\Delta\Phi_n(x) = \Delta\Phi(x_n)$, where x_n is the position of the nth pixel. As discussed by Weiner *et al.*, these sampling criteria place an upper limit of $\Delta\Phi = \pi$ between pixels, thus limiting the total amount of phase shift that can be imparted to a pulse.[12] In our experiments, this places an upper limitation of approximately 130π of total phase shift. Clearly any increase in pixel number of the SLM will allow for larger phase shifts.

In Fig. 7(a), we show the cross correlation of a pulse with a cubic chirp of $\Phi^{(3)} = 6.0 \times 10^4$ fs^3, which corresponds to a total phase shift of $\sim 12\pi$ over a 100-nm bandwidth. For comparison, a theoretical intensity profile is also shown. The experimental cross correlation (solid curve) shows remarkable fidelity and agrees well with the theoretical intensity profile for a cubic-phase modulation placed on a Gaussian-pulse spectrum (dashed curve). The temporally chirped, oscillatory prepulse is characteristic of cubic chirp in which equally temporally advanced higher- and lower-frequency components lead the pulse and interfere with each other. The effects of sampling are clearly evident in Fig. 7(b), which shows a cross correlation for a cubic chirp of $\Phi^{(3)} = 6.0 \times 10^5$ fs^3 (a phase shift of 121π). The lobe shows three distinct peaks, and a pulse substructure is seen on the trailing edge of the pulse. Undersampling is also evident in the theoretical intensity profile, in which a Gaussian spectrum was sampled at 128 points. In Fig. 8, we display linear [Fig. 8(a)] and semilog [Fig. 8(b)] plots of the cross correlation of a pulse that has a cubic chirp $\Phi^{(3)} = 2.75 \times 10^5$ fs^3 (a phase shift of 60π). Oscillations are clearly visible over the entire pulse ($\sim$1.2 ps).

Similar results are seen for quartic-phase profiles, which are shown in Fig. 9. Figure 9(a) displays an experimental cross correlation (solid curve) and a theoretical intensity profile (both plotted on a linear scale) for $\Phi^{(4)} = 1.1 \times 10^5$ fs^4 (a phase shift of 40π). Good agreement in the main pulse and the first sidelobe is seen, with deviations occurring in the wings. In particular, the experimental trace shows some asymmetry. Slight oscilla-

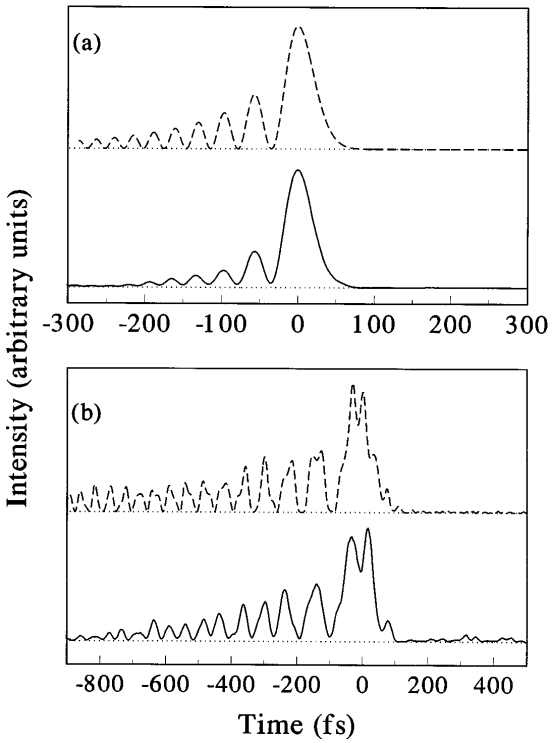

Fig. 7. Experimental cross correlations (solid curves) and numerical simulations (dashed curves) of a pulse with a cubic-phase modulation of (a) $\Phi^{(3)} = 6 \times 10^4$ fs^3 (12π), (b) $\Phi^{(3)} = 6.0 \times 10^5$ fs^3 (122π). The effects of aliasing are clearly seen in (b).

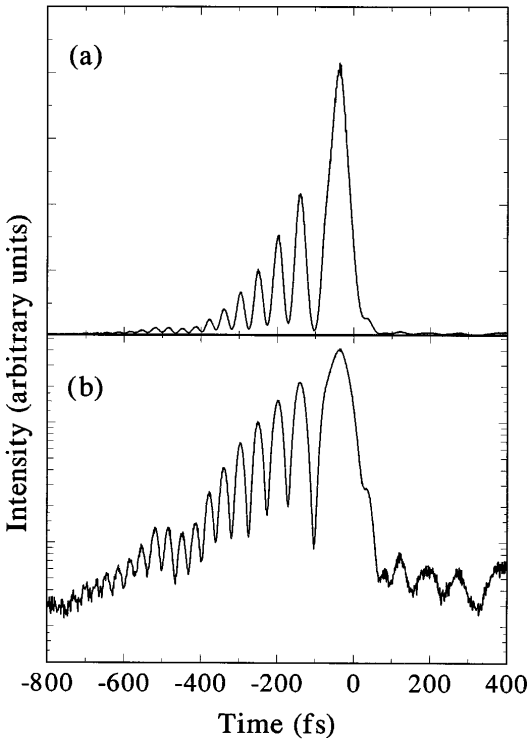

Fig. 8. (a) Cross correlation of a pulse with a cubic-phase modulation of $\Phi^{(3)} = 3.0 \times 10^5$ fs^3, (b) semilog plot of the same pulse. Oscillations are clearly visible over the entire pulse (~1.4 ps).

tions of the shaped pulse appear at negative time delays. These deviations are more pronounced in Fig. 9(b), which corresponds to a quartic phase of $\Phi^{(4)} = 1.1 \times 10^6$ fs^4 (a phase shift of 400π). These asymmetries are caused by residual cubic-phase dispersion present on the pulse and have two causes. First, imperfect alignment of the spectrum with the filter will necessarily result in the introduction of lower-order terms in the phase dispersion, i.e., $\Delta\Phi(\omega) = (1/4!)\Phi^{(4)}(\omega_0)[\omega - (\omega_0 - \Delta\omega)]^4 \approx A(\omega - \omega_0)^4 + B(\omega - \omega_0)^3$, where A and B are coefficients that depend on $\Delta\omega$. Second, any nonlinearity in the spatial frequency dispersion will also introduce lower terms into the phase expansion.

5. LIMITATIONS OF DISCRETE FOURIER-TRANSFORM PULSE SHAPING

In the previous sections, we have shown that a variety of temporal waveforms can be produced by using ultrabroad-bandwidth pulses coupled with programmable pulse-shaping techniques. In this section we ask, What are the limitations that ultrabroad bandwidths impose on pulse shaping? Large bandwidths can adversely affect the quality of shaped pulses because of (i) higher-order phase dispersion of the pulse during propagation through the shaper, which can lead to pulse broadening and loss of temporal resolution; (ii) higher-order spatial dispersion of the frequency components in the Fourier plane of the shaper, which can lead to deviations from the ideal pulse shape; and (iii) amplitude and phase filtering of the pulse from other optical elements (gratings, mirrors) in the shaper, which can also lead to pulse broadening. In this section we discuss these considerations in shaping ultrabroad-bandwidth pulses and, in particular, examine the limits of Fourier-transform techniques in shaping pulses on pulses with durations that are much shorter than those used in these experiments.

A. Effects of High-Order Spectral Dispersion

First we consider the effects of higher-order phase dispersion on the fidelity of the shaped pulse. An ultrabroad-bandwidth pulse that propagates through the pulse shaper will be broadened because of the presence of an intrinsic higher-order phase that manifests itself as a loss of temporal resolution of the individual features of the shaped pulse. The magnitude of this broadening depends on both the amount of dispersive material present in the shaper and on dispersive contributions from the diffraction gratings. In principle, any residual phase dispersion can be automatically compensated for by the adjustment of the phases of individual modulator pixels (as we have done in our cubic- and quartic-phase compensation experiments above). This permits added flexibility both for correcting intrashaper dispersion and correcting for an uncompensated higher-order phase that may be present on input pulses. Nonetheless, it is useful to consider to what extent intrinsic phase dispersion broadens short pulses and to determine the pulse durations for which this intrinsic broadening can be ignored.

Any material (SLM) contributions to positive second-order group velocity dispersion (GVD) within the shaper can be canceled if the position of the final grating is adjusted. In this case, negative GVD is introduced when the grating is moved beyond the outer focal plane of the final mirror (see Fig. 1). However, this also introduces phase dispersion at higher orders, particularly

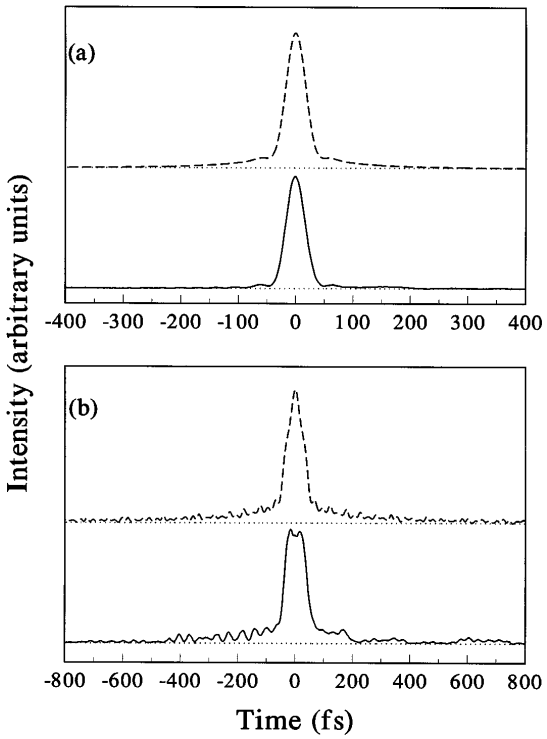

Fig. 9. Experimental cross correlations (solid curve) and numerical simulations (dashed curve) of a pulse with a quartic-phase modulation of (a) $\Phi^{(4)} = 1.1 \times 10^5$ fs^4 (40π), (b) $\Phi^{(4)} = 1.1 \times 10^6$ fs^4 (400π). The slightly asymmetric profiles are caused by residual cubic-phase dispersion.

cubic- and quartic-phase dispersions. Both the material and the grating contributions can be calculated. We can estimate the material contributions of quadratic-, cubic-, and quartic-phase distortions by using the fiber propagation parameter,[37] $\beta(\omega) = \Phi(\omega)/L$, where L is the propagation distance, and, by using the Taylor series expansion for the optical phase [Eq. (4)], we can write $\beta^{(n)}(\omega) = \Phi^{(n)}(\omega)/L = (\mathrm{d}^n\beta/\mathrm{d}\omega^n)_{\omega=\omega_0}$. The derivatives $\beta^{(n)}(\omega)$ are given in terms of the index of refraction as

$$\beta^{(2)}(\omega) = \frac{\lambda^3}{2\pi c^2}\,\frac{\mathrm{d}^2 n}{\mathrm{d}\lambda^2}\,, \tag{5a}$$

$$\beta^{(3)}(\omega) = -\frac{\lambda^4}{4\pi^2 c^3}\left(3\,\frac{\mathrm{d}^2 n}{\mathrm{d}\lambda^2} + \lambda\,\frac{\mathrm{d}^3 n}{\mathrm{d}\lambda^3}\right), \tag{5b}$$

$$\beta^{(4)}(\omega) = \frac{\lambda^5}{\pi^3 c^4}\left(\frac{3}{4}\,\frac{\mathrm{d}^2 n}{\mathrm{d}\lambda^2} + \lambda\,\frac{\mathrm{d}^3 n}{\mathrm{d}\lambda^3} + \frac{\lambda^2}{4}\,\frac{\mathrm{d}^4 n}{\mathrm{d}\lambda^4}\right). \tag{5c}$$

Using a propagation length of 4.6 mm and the Sellmeier equations for fused silica, we estimate that the SLM contributes approximately 170 fs^2, -360 fs^3, and 500 fs^4 of quadratic, cubic, and quartic phases, respectively. These phases must be added to contributions from the gratings in the shaper. Stern *et al.* have considered the propagation of subpicosecond pulses through a generalized pulse-shaping system that consists of two gratings and a unit magnification pair of focusing elements (lens).[38] From their analysis, the excess cubic- and quartic-phase terms are found to be $+430$ fs^3 and -640 fs^4, respectively. When the final grating position is set to cancel the GVD that is due to the gratings, $|\Phi_{\mathrm{grating}}{}^{(2)}(\omega)| = -|\Phi_{\mathrm{material}}{}^{(2)}(\omega)|$, the residual cubic and quartic phases can be computed as the sum of contributions from material and gratings. We experimentally measure a grating displacement of 600 μm from the focal plane, in reasonable agreement with the calculated value of 400 μm. Using the experimentally measured value for the grating phase, we estimate total cubic and quartic phases of 360 fs^3 and -100 fs^4, respectively, of our shaper. For reference, a cubic (quartic) phase of 360 fs^3 (-100 fs^4) will broaden an 12.2-fs (4.5-fs) pulse by 1 fs. When the condition that intrinsic phase dispersion can effectively be neglected when $\Delta\tau/\tau \le 1.1$ is imposed, higher-order phase dispersion can be neglected for pulse durations that exceed 12 fs. For pulses shorter than this, phase compensation by a SLM is necessary to eliminate pulse broadening. Note, however, that the phase dispersion contributions from material and gratings have opposite signs. It should therefore be possible to select the appropriate grating angle to cancel quadratic and cubic phases simultaneously.[38] In addition, our analysis does not take the effect of finite beam diameter into account, which can lead to pulse broadening across the beam radius. Such effects can in principle be minimized by the use of a one-dimensional spatial image inverter in a quadruple-pass configuration,[26] although complications that are due to the presence of SLM may exist.

B. Effects of Higher-Order Spatial Dispersion

We next consider the variation of spatial dispersion in the masking plane of the shaper and its consequence on the shaped output pulses. The pulse shaper operates by imposing a complex linear filter $M(\omega)$ on an input field spectrum $E_{\mathrm{in}}(\omega)$. However, the filtering operation is carried out in real space; hence $M(\omega)$ must be mapped from space to frequency. For small bandwidths ($\Delta\omega/\omega_0 \ll 1$), $\mathrm{d}\omega/\mathrm{d}x$ is constant, and the filter is simply a one-to-one linear map from space to frequency. For our experimental conditions, $\Delta\omega/\omega_0 = 0.16$, and the assumption of constant dispersion is invalid, as $\mathrm{d}\omega/\mathrm{d}x$ varies by 40% over the baseband spectrum of our pulses (even though $\mathrm{d}\lambda/\mathrm{d}x$ varies by only 6%). Because we are using fixed pixel size and spacing dictated by the physical characteristics of the SLM, any nonlinearity in spatial dispersion represents a deviation from the desired frequency filter.

To model the effects of spatial nonlinearity, we expand the wavelength at the masking plane to third order in a Taylor series:

$$\lambda(x) = \lambda_0 + \lambda^{(1)}(x)\Delta x + \frac{1}{2!}\,\lambda^{(2)}(x)(\Delta x)^2 + \frac{1}{3!}\,\lambda^{(3)}(x)(\Delta x)^3\,, \tag{6}$$

where $\lambda^{(n)}(x) = (\mathrm{d}^n\lambda/\mathrm{d}x^n)_{\lambda=\lambda_0}$, λ_0 is the center wavelength of the pulse, and Δx is the distance from the mask center ($x_0 = 0$). We evaluate the wavelength derivatives by considering the geometry of the shaper. Referring to Fig. 10, let f be the grating distance from the focusing optic and $\Omega = \theta_d - \theta_{d,0}$ be the difference angle between λ and λ_0. The position of λ at the masking plane is given by

$$x = f\,\tan\,\Omega\,. \tag{7}$$

The relationship between Ω and λ is obtained from the first-order grating equation:

$$d[\sin\,\theta_i + \sin(\Omega + \theta_{d,0})] = \lambda\,. \tag{8}$$

From Eqs. (7) and (8) and their respective derivatives, complicated expressions for the wavelength derivatives $\mathrm{d}^n\lambda/\mathrm{d}x^n$ can be found at arbitrary Ω. However, when evaluated at $\Omega = 0$ ($\lambda = \lambda_0$), the expressions simplify considerably:

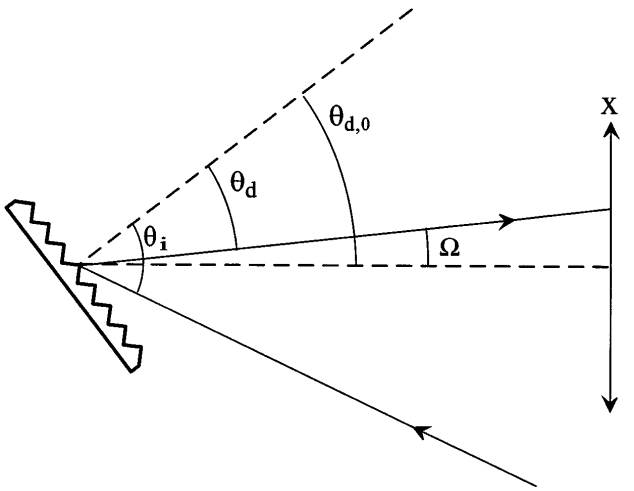

Fig. 10. Geometry for calculating the effects of higher-order spatial dispersion in the masking plane.

$$\left(\frac{d\lambda}{dx}\right)_{\lambda_0} = \frac{d\cos\theta_{d,0}}{f}, \tag{9a}$$

$$\left(\frac{d^2\lambda}{dx^2}\right)_{\lambda_0} = -\frac{d\sin\theta_{d,0}}{f^2}, \tag{9b}$$

$$\left(\frac{d^3\lambda}{dx^3}\right)_{\lambda_0} = -\frac{3d\cos\theta_{d,0}}{f^3}. \tag{9c}$$

For our experimental parameters, we find that $d\lambda/dx = 11.76$ nm/mm, $d^2\lambda/dx^2 = -5.02 \times 10^{-2}$ nm/mm^2, and $d^3\lambda/dx^3 = -2.26 \times 10^{-3}$ nm/mm^3, respectively. In Fig. 11 we plot the position-dependent wavelength by using Eq. (7) (solid line). For comparative purposes, both the linear spatial dispersion (dashed line) and the exact position calculated with Eqs. (8) and (9) are shown. Several features are apparent. First, the deviation from linearity is negligible (<5%) over a bandwidth of 120 nm, approximately the baseband spectrum of our pulses. Second, there is no difference between our derived third-order result and the exact position over 400 nm of bandwidth. This is shown clearly in the inset, which is a blowup of the bottom left-hand corner. Thus we can make an accurate assessment of the effects of nonlinear spatial dispersion on optical pulses with bandwidths that near the single-cycle limit ($\Delta\omega/\omega_0 \sim 0.3$) by using the third-order expansion.

It is crucial to note that, although the wavelength dispersion is nearly linear, the frequency dispersion is in fact quite nonlinear. This is shown clearly in Fig. 12. We note that a shaper that possesses a purely linear spatial wavelength dispersion over hundreds of nanometers of bandwidth will necessarily possess a significant amount of nonlinear frequency spatial dispersion. For a device that has a fixed pixel size (such as a liquid-crystal SLM), this results in a variation in the amount of frequency that is transmitted through each pixel. Rigorously, the spectral filter including nonlinear dispersion is given by[39]

$$M(\omega) = \left(\frac{2}{\pi {w_0}^2}\right)^{1/2} \int dx M(x) \exp\left\{\frac{-2(x - f[\omega])}{{w_0}^2}\right\}, \tag{10}$$

where $M(x)$ is the physical mask, w_0 is the electric-field radius at the masking plane, and the nonlinear spatial dispersion is

$$f(\omega) = \frac{dx}{d\omega}\omega + \frac{1}{2!}\frac{d^2x}{d\omega^2}\omega^2 + \frac{1}{3!}\frac{d^3x}{d\omega^3}\omega^3 + \cdots. \tag{11}$$

For a discrete N pixel filter, the physical mask can be written as[12]

$$M(x) = \left[C(x)\sum_{n=-N/2}^{N/2-1}\delta(x - n\delta x)\right] * \mathrm{rect}\left(\frac{x}{\delta x}\right), \tag{12}$$

where $C(x)$ is the continuous spatial mask that corresponds to the desired frequency filter, assuming linear spatial dispersion, δx is the physical width of the pixel, the function $\mathrm{rect}(x) = 1$ for $|x| \le 1/2$ and 0 otherwise, and * is the convolution operator. With Eqs. (10) and (12), under the assumption that the field radius (spot size) at the masking plane is much smaller than the pixel width (as in our case), the spectral filter becomes

$$M(\omega) = \left\{C[f(\omega)]\sum_{n=-N/2}^{N/2-1}\delta[f(\omega) - n\delta x]\right\} * \mathrm{rect}\left[\frac{f(\omega)}{\delta x}\right]. \tag{13}$$

From Eq. (13), two features are noteworthy. First, the delta-function terms explicitly show that the frequency is not sampled at equal intervals. Second, as $f(\omega)/\delta x$ varies with frequency, the amount of transmitted frequency per pixel is not constant.

To examine these effects on the fidelity of shaped ultrabroad-bandwidth pulses, we have performed simulations on pulses with 5-fs duration in which the nonlinear spatial dispersion is incorporated in the filtering process. We first compute the continuous spatial filter $C(x)$ that corresponds to our desired frequency filter under the assumption of a purely linear frequency-space map. The actual frequency-dependent filter $M(\omega)$ that samples the pulse spectrum [Eq. (13)] is constructed by the mapping of space to frequency (including nonlinear spatial dispersion) directly from the wavelength expansion [Eq. (6)] and $\omega(x) = 2\pi c/\lambda(x)$. We include the effect of pixelation by discretizing and sampling the input field spectrum at the 128 appropriate points in frequency space according to Eq. (13). This corresponds to a frequency range (at the center frequency ω_0) of 2.5 THz/pixel and a corresponding

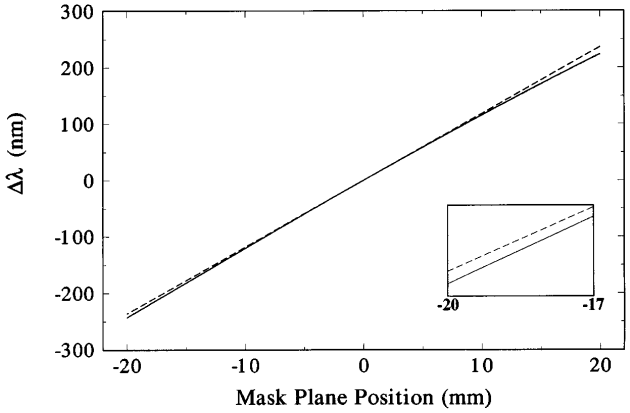

Fig. 11. Spatial wavelength dispersion in the masking plane of the shaper, showing linear dispersion (dashed curve) and third-order dispersion (solid curve). The exact position of the wavelength in the masking plane is identical to the third-order result over this wavelength.

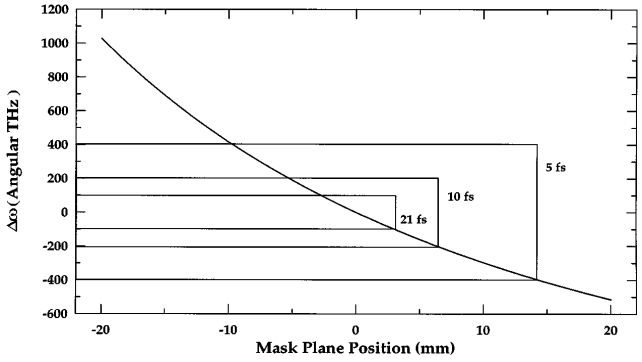

Fig. 12. Spatial frequency dispersion in the masking plane of the shaper, plotted in angular terahertz, obtained from the third-order wavelength result. FWHM bandwidths for 21, 10, and 5 fs are shown for reference.

(linear) temporal window of 400 fs. The shaped intensity profile of the pulse is computed by[30]

$$I(t) = \frac{1}{(2\pi)^2} \int \mathrm{d}\omega' \exp(i\omega' t) \int \mathrm{d}\omega E_{\mathrm{out}}(\omega)^* \times E_{\mathrm{out}}(\omega + \omega'), \quad (14)$$

where the shaped field is given by $E_{\mathrm{out}}(\omega) = E_{\mathrm{in}}(\omega)M[\omega(x)]$. For these simulations, we use a Gaussian intensity spectrum of the form $I_{\mathrm{in}}(\omega) = E_0{}^2 \exp(-4 \ln 2\ \omega^2/\Delta\omega_{\mathrm{FWHM}}{}^2)$ where $\Delta\omega = 88$ THz and corresponds to a 5-fs pulse. To model the finite spatial extent of our hypothetical SLM, the intensity spectrum is truncated at four *e*-foldings. In this manner, ringing and feature broadening associated with hard spectral apertures are minimized. {However, because the wavelength dispersion [Eq. (6)] was computed with the parameters of our current shaper, the physical size of our hypothetical SLM must be ~40 mm to accommodate this bandwidth.} Three representative filters are considered in our simulations: a double-slit amplitude filter, an *M*-sequence phase filter, and $\sin(\omega)/\omega$ phase and amplitude filter.

Results for the double-slit filter are shown in Fig. 13. Selecting two separate, phase-locked portions of the spectrum results in a temporal beat note with a period that corresponds to the inverse mean frequency separation of the spectra. For ordinary (linear) filtering, the width of the temporal envelope would correspond to the inverse of the transmitted frequency range of the slit. In each of these simulations, the spatial filter was constructed to have slits of equal physical width centered about the physical position of the central wavelength. When transformed into frequency space, the spatial nonlinearity asymmetrically positions the slits with respect to the spectrum. In addition, the amount of transmitted frequency range is different in each slit. Figure 13(a) displays the computed output temporal profile for a mean frequency separation of 66.8 THz, which corresponds to a pulse period of 15 fs. In this simulation, the left (right) slit was positioned at −6 mm (6 mm) with widths of 2 mm. The transmitted frequency range through the left (right) slit was 13.6 THz (9.4 THz). The width of the temporal envelope is 78 fs, which is nearly the value expected for the wider slit width of 13.6 THz. A series of isolated pulses are seen, and pulse positions correspond to their expected values. Figure 13(b) displays the output pulse profile for a mean frequency separation of 138.1 THz and a pulse spacing of 7.2 fs. Here, the left (right) slit was positioned at −12 mm (12 mm) with widths of 6 mm, and the transmitted frequency range through the left (right) slit was 52.3 THz (22.6 THz). Again we find that the pulses are isolated in their appropriate positions with a temporal envelope width of 27.5 fs.

In Fig. 14, results for a length 7 *M*-sequence with a 5.0-fs input pulse are shown for a $\delta F = 62.5$ THz train. The *M*-sequence was discussed in Section 3 above and has been previously used for shaping pulse trains.[30] For these simulations, $\Delta\phi = 1.1\pi$ and six repetitions of the *M*-sequence spanned the spectrum. The quality of the synthesized pulse train has degraded with respect to a train simulated assuming purely linear frequency dispersion (shown as the offset dashed curve). The central pulse in the train maintains its width, but the temporally shifted pulses are broadened by as much as a factor of 2 and deteriorate beyond the third pulse in the trains. Evidence for this is present in our experimental cross correlations of a 23.5-THz train shown in Fig. 6(c).

Finally, in Fig. 15 we display simulations for temporal square pulses of 50-, 100-, and 300-fs durations. Here the filter chosen was $\sin(\pi x/x_0)/(\pi x/x_0)$ with $x_0 = [T(\mathrm{d}\nu/\mathrm{d}x)_{\nu=\nu_0}]^{-1}$, where T is the duration of the square pulse and $(\mathrm{d}\nu/\mathrm{d}x)_{\nu=\nu_0}$ is the frequency dispersion at the center frequency of the pulse. Again, ideal square pulses are shown as the offset dashed curve. For the 50-fs square pulse [Fig. 15(a)], slight deviations appear along the leading and the trailing edges of the pulses, including a 15% overshoot of the main plateau and a slight broadening of the rise and fall time from 5 to 8 fs. Both of these effects grow as the square pulse duration is increased, with a 100- (300-) fs square pulse [Figs. 15(b) and 15(c)] suffering a 13- (25-) fs broadening and a 25% (34%) overshoot of the main plateau. In the case of the 300-fs pulse, ringing appears on both the leading and the trailing edge of the pulses. In all cases, however, the overall character of the square pulse is preserved.

Our simulations suggest that although nonlinear spatial effects play a minimal role in simple filters (such as double slits) on 5-fs time scales, they can affect the fidelity of complicated waveforms (such as square pulses) and in the worst case render a seriously degraded waveform (as evidenced in our simulations of *M*-sequence filters). Specifically, as the square pulse illustrates, the quality of the pulse degrades with increasing waveform duration. One possible cause of these effects can be un-

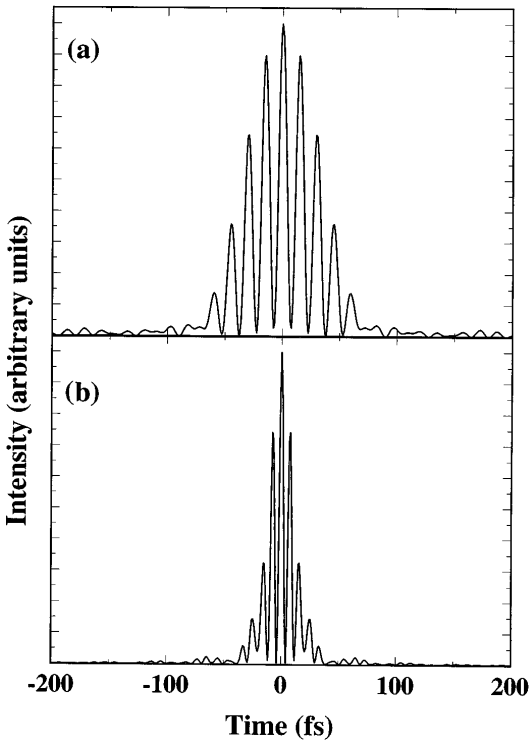

Fig. 13. Numerical simulations of (a) 66.8-THz, (b) 138.1-THz pulse trains that incorporate the effects of higher-order spatial dispersion, assuming a transform-limited 5-fs input pulse. These trains were synthesized by the use of an amplitude mask that consisted of two slits of equal spatial dimension centered about $x = 0$ in the masking plane.

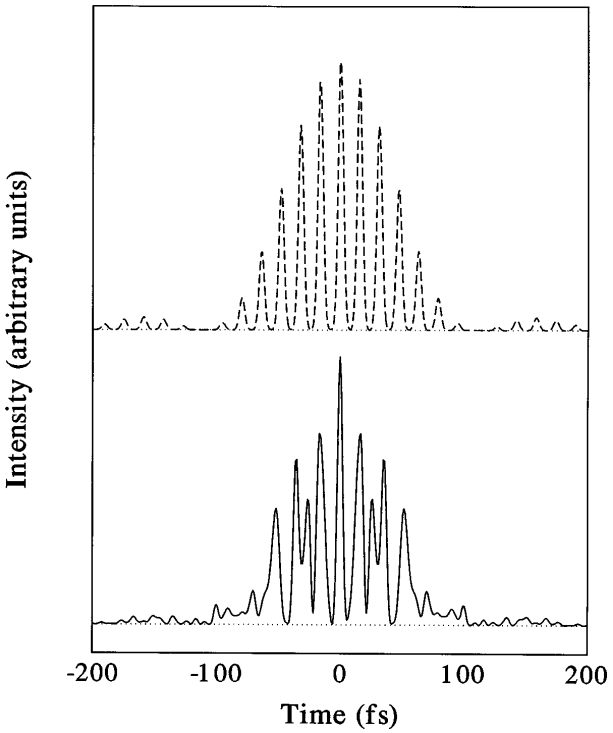

Fig. 14. Numerical simulation of a 62.5-THz pulse train (solid curve) that shows the effects of higher-order spatial dispersion, synthesized with a length 7 *M*-sequence phase mask. The fidelity of this train is significantly degraded with respect to a train synthesized assuming only linear frequency dispersion in the masking plane (dashed curve).

derstood by considering the variance of the transmitted frequency as a function of pixel position. For a filter with purely linear spatial dispersion (assuming $w_0 \ll \delta x$), the temporal window available for shaping is given by $1/\delta\omega$, where $\delta\omega$ is the transmitted frequency per pixel. For large bandwidths, however, $1/\delta\omega$ varies considerably over the pulse bandwidth. In our simulations, 1.4 THz $< \delta\omega <$ 3.7 THz at two *e*-foldings, which effectively reduces the shaping window to ~270 fs. Moreover, the simulated *M*-sequence pulse train displays degradation well within the 270-fs window, indicating that nonlinear sampling plays an important role. Because the *M*-sequence train is constructed by the phase shifting of specific frequencies to interfere constructively at the appropriate pulse positions, incorrect sampling of the frequency will compromise the interference and necessarily degrade the waveform. Therefore, for the most general waveform, the effects of nonlinear spatial dispersion will need to be compensated for. If the optical bandwidths of the pulses are known *a priori*, this could be accomplished in systems that utilize fixed masks simply if the filter is designed to incorporate the frequency dispersion directly. This has the disadvantage of the need to fabricate, replace, and realign a new mask for each new set of waveforms. Similarly, one could design a pixelated SLM device that exactly incorporates the frequency-to-space nonlinear mapping by having unevenly spaced pixels with varied physical dimensions such that the amount of frequency transmitted per pixel is constant over the entire bandwidth of the pulse. This would require the fabrication of a specialized device. A third possibility is to increase the frequency resolution by increasing the number of pixels. This, however, presents disadvantages in any implementation. In an SLM, the decreased pixel size would result in a filter that convolves the desired filter with the intensity profile of the input beam.[39] An acousto-optic modulator[14] would overcome this problem by virtue of its quasi-continuous pixelation. However, the wavelength variation of the Bragg diffraction angle and diffraction efficiency that necessarily accompany ultrabroad-bandwidth pulses would need to be addressed before this method could be applied. A fourth possibility is simply to assign the correct phase to the appropriate (nonlinear) spatial position. This guarantees that the spectrum is sampled correctly.

C. Effects Of Extraneous Amplitude Filters

Finally, we briefly consider amplitude filtering effects that can compromise the fidelity of shaped wide-bandwidth pulses. Some amplitude shaping can be expected by the diffraction gratings within the shaper, as diffraction efficiency varies both with wavelength and polarization. We have not characterized the spectral transmission of our shaper; however, we note that for 13-fs

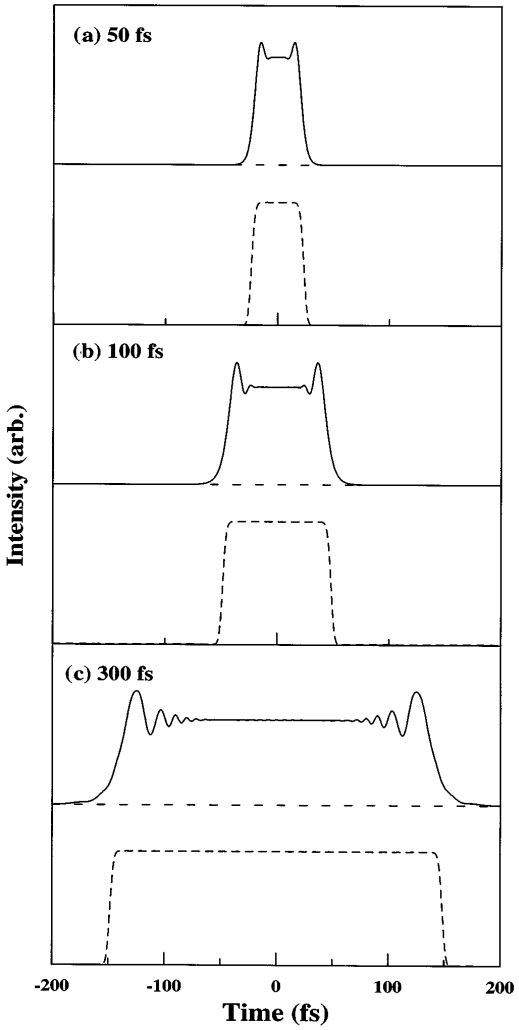

Fig. 15. Numerical simulations of (a) 50-fs, (b) 100-fs, (c) 300-fs square pulses (solid curve) synthesized with $\sin(\pi x/x_0)/(\pi x/x_0)$ phase and amplitude filters. For comparison, ideal square pulses (dashed curve) synthesized assuming linear frequency dispersion are also displayed.

pulses, these effects are minimal based on our measured unshaped cross correlations. For shorter pulses with correspondingly broader bandwidths, these effects may become important, particularly if the shaper is operated in a multipass configuration. Typically, grating efficiencies can be as broad as several hundred nanometers for high groove-density gratings. However, grating bandwidths diminish as groove density decreases and may present problems for pulses with durations that approach single-cycle limits.

6. CONCLUSION

We have demonstrated that spectral domain femtosecond pulse-shaping techniques can be easily applied to ultrabroad-bandwidth pulses with durations as short as 13 fs. A variety of temporal profiles has been generated by the use of a programmable spatial light phase modulator within a dispersion-free pulse-shaping apparatus. Although we have performed phase filtering in these experiments, amplitude and combined phase and amplitude filtering should be possible with similar temporal resolution. We have also demonstrated the feasibility of using a SLM-based shaper as a high-order phase dispersion compensator for ultrabroad-bandwidth femtosecond pulses. From the numerical modeling of the effects of phase dispersion and spatial dispersion within the shaper, we conclude that these methods can be extended to pulses with durations that approach a single optical cycle, provided that filters that adequately account for the nonlinear spatial dispersion in the masking plane are designed.

ACKNOWLEDGMENTS

This research was supported by the National Science Foundation (ECS9409297). The authors thank Henry Kapteyn and Christopher Barty for their helpful suggestions concerning operation of the mode-locked Ti:sapphire laser.

REFERENCES

1. A. M. Weiner, J. P. Heritage, and E. M. Kirschner, "High-resolution femtosecond pulse shaping," J. Opt. Soc. Am. B **5,** 1563 (1988).
2. A. M. Weiner, J. P. Heritage, R. J. Hawkins, R. N. Thurston, E. M. Kirschner, D. E. Leaird, and W. J. Tomlinson, "Experimental observation of the fundamental dark soliton in optical fibers," Phys. Rev. Lett. **61,** 2445 (1988).
3. A. M. Weiner, D. E. Leaird, G. P. Wiederrecht, and K. A. Nelson, "Femtosecond pulse sequences used for optical control of molecular motion," Science **247,** 1317 (1990); "Femtosecond multiple-pulse impulsive stimulated Raman scattering spectroscopy," J. Opt. Soc. Am. B **8,** 1264 (1991).
4. H. Rabitz and S. Shi, "Optimal control of molecular motion: making molecules dance," in *Vibrational Spectroscopy*, J. Bowman, ed. (Jai, Greenwich, Conn., 1991), Vol. 1, Part A, p. 187.
5. W. S. Warren, H. Rabitz, and Mohammed Dahleh, "Coherent control of quantum mechanics: the dream is alive," Science **259,** 1581 (1993).
6. Y. Yan, R. E. Gillilan, R. M. Whitnell, K. R. Wilson, and S. Mukamel, "Optical control of molecular dynamics: Liouville-space theory," J. Chem. Phys. **97,** 2320 (1993).
7. B. Kohler, J. L. Krause, R. M. Whitnell, K. R. Wilson, V. V. Yakovlev, and Y. Yan, "Quantum control of vibrational dynamics with tailored light pulses," in *Ultrafast Phenomena IX*, G. A. Mourou, A. H. Zewail, P. F. Barbara, and W. H. Knox, eds. (Springer-Verlag, Berlin, 1994), p. 44.
8. P. C. M. Planken, I. Brener, M. C. Nuss, M. S. C. Lou, and S. L. Chuang, "Coherent control of terahertz charge oscillations in a coupled quantum well using phase-locked optical pulses," Phys. Rev. B **48,** 4903 (1993).
9. A. M. Weiner, "Enhancement of coherent charge oscillations in coupled quantum wells by femtosecond pulse shaping," J. Opt. Soc. Am. B **11,** 2480 (1994).
10. P. Hyldgaard, G. D. Sanders, and D. H. Reitze, "Coherent optical control of electron dynamics in asymmetric double quantum wells in the nonimpulsive regime," presented at the Annual Meeting of the Optical Society of America, Dallas, Tx., October 1994.
11. D. Umstadter, E. Esarey, and J. Kim, "Nonlinear plasma waves resonantly driven by optimized laser pulse trains," Phys. Rev. Lett. **72,** 1224 (1994).
12. A. M. Weiner, D. E. Leaird, J. S. Patel, and J. R. Wullert, "Programmable femtosecond pulse shaping by use of a multielement liquid-crystal phase modulator," Opt. Lett. **15,** 326 (1990); "Programmable shaping of femtosecond optical pulses by use of 128-element liquid crystal phase modulator," J. Quantum Electron. **28,** 908 (1992).
13. M. A. Wefers and K. A. Nelson, "Programmable phase and amplitude femtosecond pulse shaping," Opt. Lett. **18,** 2032 (1993).
14. C. W. Hillegas, J. X. Tull, D. Goswami, D. Strickland, and W. Warren, "Femtosecond laser pulse shaping by use of microsecond radio-frequency pulses," Opt. Lett. **19,** 737 (1994).
15. A. M. Weiner, D. E. Leaird, D. H. Reitze, and E. G. Paek, "Spectral holography of shaped femtosecond pulses," Opt. Lett. **17,** 224 (1992); "Femtosecond spectral holography," IEEE J. Quantum Electron. **28,** 2251 (1992).
16. A. M. Weiner and D. E. Leaird, "Femtosecond signal processing by second-order spectral holography," Opt. Lett. **19,** 123 (1994).
17. M. C. Nuss, M. Li, T. H. Chiu, A. M. Weiner, and A. Partovi, "Time-to-space mapping of femtosecond pulses," Opt. Lett. **19,** 664 (1994).
18. D. H. Reitze, A. M. Weiner, and D. E. Leaird, "Shaping of wide bandwidth, 20 fsec optical pulses," Appl. Phys. Lett. **61,** 1260 (1992).
19. D. H. Reitze, A. M. Weiner, and D. E. Leaird, "Spatial soliton pulse compression," Opt. Lett. **16,** 1409 (1991).
20. J. Zhou, G. Taft, C. Shi, H. C. Kapteyn, and M. C. Murnane, "Sub-10 fs pulse generation in Ti:sapphire: capabilities and ultimate limits," in *Ultrafast Phenomena IX*, G. A. Mourou, A. H. Zewail, P. F. Barbara, and W. H. Knox, eds. (Springer-Verlag, Berlin, 1994), p. 39.
21. I. P. Christov, M. M. Murnane, H. C. Kapteyn, J. P. Zhou, and C. P. Huang, "Fourth-order dispersion-limited solitary pulses," Opt. Lett. **19,** 1465 (1994).
22. J. D. Kmetec, J. J. Macklin, and J. F. Young, "0.5-TW, 125-fs Ti:sapphire laser," Opt. Lett. **16,** 1001 (1991).
23. A. Sullivan, H. Hamster, H. C. Kapteyn, S. Gordon, W. White, H. Nathel, R. J. Blair, and R. W. Falcone, "Multiterawatt, 100-fs laser," Opt. Lett. **16,** 1406 (1991).
24. C. P. Barty, C. L. Gordon, and B. E. Lemoff, "Multiterawatt 30-fs ti-sapphire laser system," Opt. Lett. **18,** 1442 (1994).
25. W. E. White, F. G. Patterson, R. L. Combs, D. F. Price, and R. L. Shepherd, "Compensation of higher-order frequency-dependent phase terms in chirped-pulse amplification systems," Opt. Lett. **18,** 1343 (1993).
26. B. E. Lemoff and C. P. J. Barty, "Quintic-phase-limited, spatially uniform expansion and recompression of ultrashort optical pulses," Opt. Lett. **18,** 1651 (1993).
27. M. T. Asaki, C. P. Huang, D. Garvey, J. P. Zhou, H. C. Kapteyn, and M. M. Murnane, "Generation of 11-fs pulses from a self-mode-locked Ti-sapphire laser," Opt. Lett. **18,** 977 (1993).
28. See, for example, E. Hecht and A. Zajac, *Optics* (Addison-Wesley, Reading, Mass., 1976), p. 323.
29. J. E. Rothenberg, D. Grischkowsky, and A. C. Balant, "Observation of the formation of the 0π pulse," Phys. Rev. Lett. **53,** 552 (1984).
30. A. M. Weiner and D. E. Leaird, "Generation of terahertz-

rate trains of femtosecond pulses by phase-only filtering," Opt. Lett. **15,** 51 (1990).
31. See, for example, W. H. Press, S. A. Teukolsky, W. T. Vettering, and B. P. Flannery, *Numerical Recipes* (Cambridge U. Press, Cambridge, 1992), Chap. 10.
32. A. M. Weiner, S. Oudin, D. E. Leaird, and D. H. Reitze, "Shaping of femtosecond pulses using phase-only filters designed by simulated annealing," J. Opt. Soc. Am. B **10,** 1112 (1993).
33. E. B. Treacy, "Optical pulse compression with diffraction gratings," IEEE J. Quantum Electron. **5,** 454 (1969).
34. R. L. Fork, O. E. Martinez, and J. P. Gordon, "Negative dispersion using pairs of prisms," Opt. Lett. **9,** 150 (1984).
35. R. L. Fork, C. H. Brito-Cruz, P. C. Becker, and C. V. Shank, "Compression of optical pulses to six femtoseconds using cubic phase compensation," Opt. Lett. **12,** 483 (1987).
36. J. P. Zhou, C. P. Huang, C. Y. Shi, M. M. Murnane, and H. C. Kapteyn, "Generation of 21-fs millijoule-energy pulses by use of Ti-sapphire," Opt. Lett. **19,** 126 (1994).
37. See, for example, G. P. Agrawal, "*Nonlinear Fiber Optics* (Academic, Boston, 1989), Chap. 1.
38. M. Stern, J. P. Heritage, and E. W. Chase, "Grating compensation of 3rd-order fiber dispersion," IEEE J. Quantum Electron. **28,** 2742 (1992).
39. R. W. Thurston, J. P. Heritage, A. M. Weiner, and W. J. Tomlinson, "Analysis of picosecond pulse shape synthesis by spectral masking in a grating pulse compressor," IEEE J. Quantum Electron. **22,** 682 (1986).